

MIT Open Access Articles

*Resolving the nature of electronic excitations
in resonant inelastic x-ray scattering*

The MIT Faculty has made this article openly available. **Please share** how this access benefits you. Your story matters.

Citation: Kang, M., et al. "Resolving the Nature of Electronic Excitations in Resonant Inelastic X-Ray Scattering." *Physical Review B*, vol. 99, no. 4, Jan. 2019. © 2019 American Physical Society

As Published: <http://dx.doi.org/10.1103/PhysRevB.99.045105>

Publisher: American Physical Society

Persistent URL: <http://hdl.handle.net/1721.1/121060>

Version: Final published version: final published article, as it appeared in a journal, conference proceedings, or other formally published context

Terms of Use: Article is made available in accordance with the publisher's policy and may be subject to US copyright law. Please refer to the publisher's site for terms of use.



Resolving the nature of electronic excitations in resonant inelastic x-ray scatteringM. Kang,¹ J. Pellicciari,¹ Y. Krockenberger,² J. Li,¹ D. E. McNally,³ E. Paris,³ R. Liang,^{4,5} W. N. Hardy,^{4,5} D. A. Bonn,^{4,5} H. Yamamoto,² T. Schmitt,³ and R. Comin^{1,*}¹*Department of Physics, Massachusetts Institute of Technology, Cambridge, Massachusetts 02139, USA*²*NTT Basic Research Laboratories, NTT Corporation, 3-1 Morinosato-Wakamiya, Atsugi, Kanagawa 243-0198, Japan*³*Research Department Synchrotron Radiation and Nanotechnology, Paul Scherrer Institut, 5232 Villigen PSI, Switzerland*⁴*Department of Physics and Astronomy, University of British Columbia V6T 1Z1, Canada*⁵*Quantum Matter Institute, University of British Columbia V6T 1Z4, Canada*

(Received 18 October 2018; revised manuscript received 13 December 2018; published 2 January 2019)

The study of elementary bosonic excitations is essential toward a complete description of quantum electronic solids. In this context, resonant inelastic x-ray scattering (RIXS) has recently risen to becoming a versatile probe of electronic excitations in strongly correlated electron systems. The nature of the radiation-matter interaction endows RIXS with the ability to resolve the charge, spin, and orbital nature of individual excitations. However, this capability has been only marginally explored to date. Here, we demonstrate a systematic method for the extraction of the character of excitations as imprinted in the azimuthal dependence of the RIXS signal. Using this approach, we resolve the charge, spin, and orbital nature of elastic scattering, (para-)magnon/bimagnon modes, and higher-energy *dd* excitations in magnetically ordered and superconducting copper oxide perovskites (Nd_2CuO_4 and $\text{YBa}_2\text{Cu}_3\text{O}_{6.75}$). Our method derives from a direct application of scattering theory, enabling us to deconstruct the complex scattering tensor as a function of energy loss. In particular, we use the characteristic tensorial nature of each excitation to precisely and reliably disentangle the charge and spin contributions to the low-energy RIXS spectrum. This procedure enables to separately track the evolution of spin and charge spectral distributions in cuprates with doping. Our results demonstrate a new capability that can be integrated into the RIXS toolset and that promises to be widely applicable to materials with intertwined spin, orbital, and charge excitations.

DOI: [10.1103/PhysRevB.99.045105](https://doi.org/10.1103/PhysRevB.99.045105)**I. INTRODUCTION**

The emergence of collective excitations associated with different often coupled degrees of freedom is a common trait in strongly interacting systems. The detailed nature of the fundamental interactions is reflected not only in the momentum-energy spectrum, but also in the character of these emerging excitations. In recent years, resonant inelastic x-ray scattering (RIXS) has earned a leading role in the study of electronic excitations in quantum materials, thanks to improved energy resolutions enabling access to low-energy excitations [1–16]. In addition to its distinctive features including elemental selectivity, bulk sensitivity, and compatibility with small samples or thin films, RIXS covers an extended kinematic range in energy and momentum, complementing prominent scattering techniques, such as neutron scattering, electron energy loss spectroscopy, and Raman/Brillouin scattering [1]. At the same time, RIXS is sensitive to a broad array of excitations arising from the spin, charge, orbital, and lattice degrees of freedom. However, the assignment of individual excitations is intricate and has sometimes been elusive, leaving the full potential of RIXS untapped [17–23].

The complexity of the interpretation of RIXS spectra has represented a constant challenge for experimental and theoret-

ical RIXS studies on cuprate [17–22]. In cuprates, the evolution of the low-energy excitations from the antiferromagnetic parent insulator to the carrier-doped superconductor is a key piece in the grand puzzle of high-temperature superconductivity [24]. RIXS has detected persisting spin excitations across the phase diagram of the cuprates, producing experimental evidences to be accounted for in magnetic pairing theories [3,4]. However, the radiation-matter interaction is extremely complicated and allows the observation of several degrees of freedom whose nature is hard to disentangle experimentally leading to possible different interpretation of the experimental data [17]. Subsequently, the various interesting theories have been proposed: Some calculations argue that RIXS actually probes the spin dynamical structure factor in doped cuprate (i.e., paramagnon excitation) [21,22], whereas others suggest the incoherent particle-hole excitations arising from the band-structure effect as an origin of the experimental RIXS spectra in metallic cuprates [18,19]. The full validation of these scenarios rests on the experimental capability to separately track down the doping evolution of the spin and charge susceptibility.

In other materials, it is the orbital degrees of freedom that plays an essential role in determining the electronic ground-state and low-lying excitations. This class of strongly correlated systems includes orbital-ordered nickelates and manganites, Fe-based superconductors, cobaltates, and spin-orbit coupled *5d* oxides [15,16,25–33]. In these materials, the

*rcomin@mit.edu

orbital degrees of freedom are dynamically active (and often coupled to spin and charge) and contribute to the spectrum of low-energy excitations, thus complicating the interpretation of RIXS spectra. Most importantly, the polarization analysis, besides requiring additional experimental components, provides only limited information in these cases since the scattering matrix for orbital excitations is typically more asymmetric (see Appendix A) than the charge and spin channels. These considerations underscore the importance to develop a systematic method to resolve the nature and character of individual excitations encoded in the RIXS spectra.

RIXS is a second-order interaction process governed by a polarization-dependent cross section which can be derived from the Kramers-Heisenberg formula [1,10]. Most importantly, in the RIXS process, the character of each excitation is uniquely imprinted onto a distinctive form of the scattering tensor, which is ultimately determined by the matrix elements of the interaction (electric dipole) operator. The scattering tensor can be partly resolved by measuring the RIXS signal as a function of the polarization of incident (σ_{in}/π_{in} : perpendicular/parallel to the scattering plane) and scattered (σ_{out}/π_{out}) photon beams for a total of four polarization channels ($\sigma_{in}-\sigma_{out}$, $\sigma_{in}-\pi_{out}$, $\pi_{in}-\sigma_{out}$, and $\pi_{in}-\pi_{out}$). Full polarization analysis is therefore often insightful [20,34,35] but ultimately insufficient to resolve the full (3×3) scattering tensor especially in systems with complex orbital physics where all components are nonzero and the tensor is asymmetric.

In this paper, we apply a special procedure to resolve the RIXS scattering tensor *at a given momentum transfer*, and correspondingly uncover the nature of excitations as a function of both energy and momentum. Our experimental approach relies on the use of an azimuthal scanning geometry where the sample is placed on a wedged holder as shown in Fig. 1(a). This geometry, owing to the collinearity of the azimuthal rotation axis to the direction of momentum transfer, ensures that the probed wave vector remains fixed (both in-plane \mathbf{Q}_{\parallel} and out-of-plane \mathbf{Q}_{\perp} components) for all values of the azimuthal angle (ϕ). At each azimuthal angle, different combinations of the tensor components are selected so that the symmetry of scattering tensor is imprinted onto the azimuthal dependence of RIXS signal. This probing scheme is often used in resonant elastic x-ray scattering experiments and is here demonstrated for inelastic processes [36,37]. In our experiment, an ostensible variation of the RIXS signal can be observed as a function of ϕ and, most importantly, the intensity modulation is different for each spectral component, reflecting the symmetry of the underlying scattering tensor [Fig. 1(b)]. We applied this method to resolve the charge, spin, and orbital nature of elastic scattering, magnon and multimagnon, and dd excitations in cuprate compounds Nd_2CuO_4 (NCO) and $\text{YBa}_2\text{Cu}_3\text{O}_{6.75}$ (YBCO). The excellent agreement between theory and experiment for a wide range of excitations confirms the ability of our method to accurately disentangle the charge, spin, and orbital contributions to elementary excitations in solids.

II. METHODS

Thin films of antiferromagnetic Nd_2CuO_4 (AF-NCO) and superconducting Nd_2CuO_4 (SC-NCO) were grown by molec-

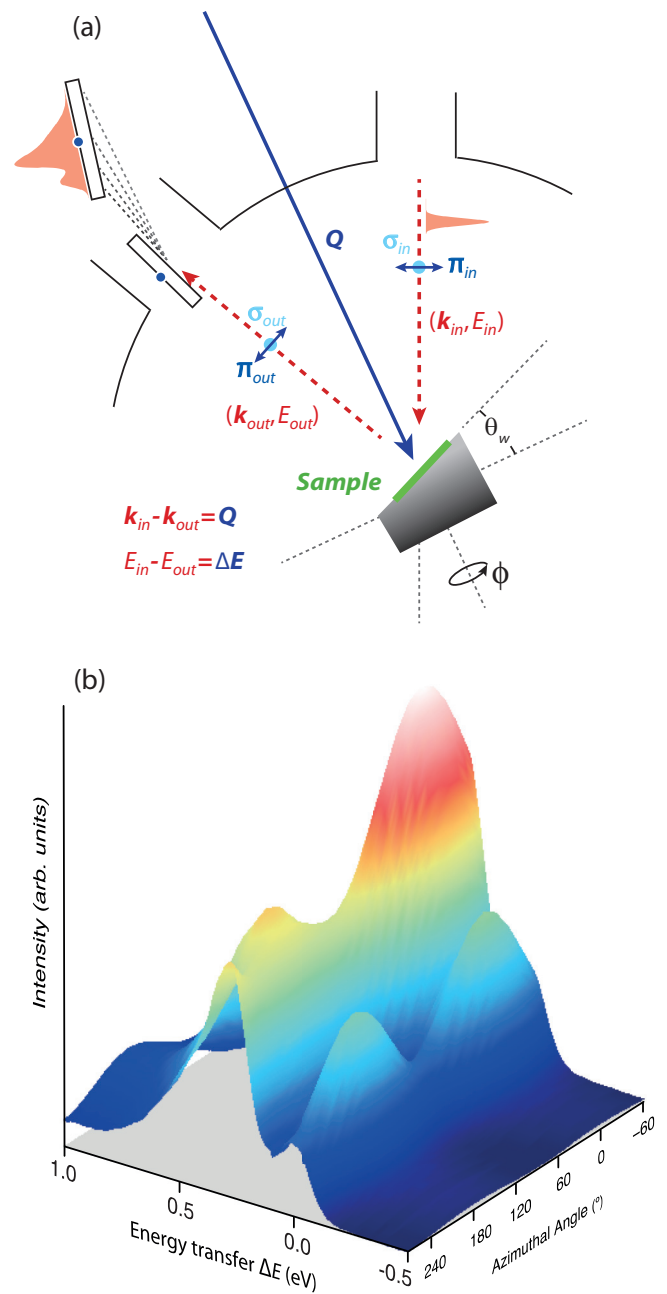


FIG. 1. (a) Schematic of the scattering geometry for azimuthal angle-dependent RIXS experiments. The orientation of the sample as in the figure defines the zero of the azimuthal angle ϕ . (b) Surface plot of the azimuthal dependence of the low-energy RIXS spectrum of antiferromagnetic Nd_2CuO_4 (AF-NCO) measured with incoming σ polarization.

ular beam epitaxy under ultrahigh vacuum using Nd and Cu metal sources and atomic oxygen generated *in situ* from a rf oxygen source [38]. Reflection high-energy electron diffraction and electron impact emission spectroscopy were used to monitor and control the growth of Nd_2CuO_4 films on (001) SrTiO_3 substrates in real time. High-resolution reciprocal space mapping data clearly show that the NCO films (100 nm) are grown fully relaxed. As-grown NCO films (AF-NCO) were rapidly cooled after the growth under ultrahigh

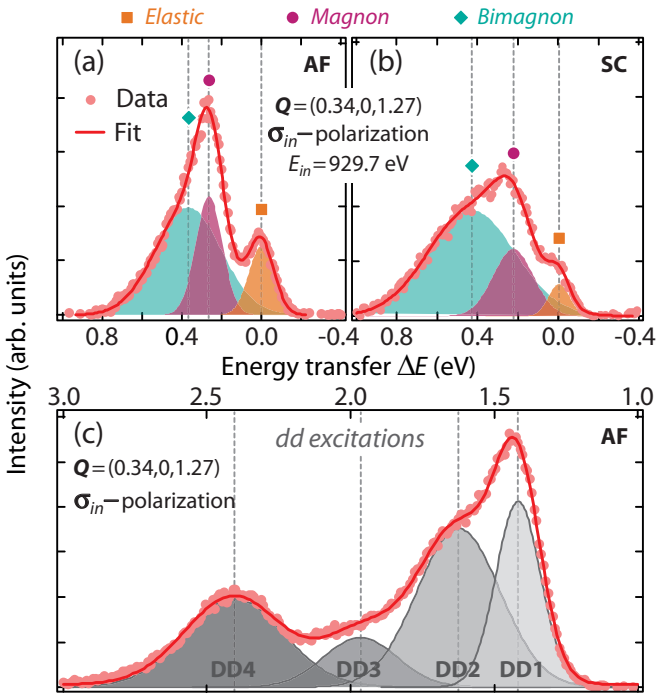


FIG. 2. (a) and (b) Low-energy RIXS spectra of AF-NCO and SC-NCO after subtraction of a linear background. Orange, magenta, and green Gaussian peaks represent the elastic, (para-)magnon, and bimagnon peaks, respectively. (c) dd -excitation regions of AF-NCO. Data are measured at $\phi = 0^\circ$ with incoming σ polarization.

vacuum, whereas SC-NCOs were subject to a two-step annealing process [39]. Superconductivity was confirmed by electric transport and magnetization measurements. The YBCO single crystals were grown by a self-flux method using BaZrO₃ crucibles [40].

The RIXS data were collected at the ADRESS beamline of the Swiss Light Source at the Paul Scherrer Institut, Villigen PSI, Switzerland [41,42]. The combined energy resolution was approximately 130 meV (determined by recording the elastic scattering from a carbon-filled acrylic tape), and the scattering angle was fixed at 130° . The samples were mounted on a wedged-sample holder to align the azimuthal rotation axis with the direction of the probed wave-vector \mathbf{Q} . The azimuthal angle $\phi = 0^\circ$ is defined so as to have the a and c crystallographic axes spanning the scattering plane. The azimuthal series ranges from -60° to 270° in 15° steps, covering more than 90% of the full 360° rotation. All measurements were performed at 15 K using a liquid-He cryostat. The excitation energy for RIXS measurements has been set to the maximum of the Cu L_3 absorption line and has been regularly monitored during the experiment. The data reported here have been normalized to the acquisition time as the intensity of the incoming beam was determined to be constant from monitoring the drain current on the last optical elements before the sample.

III. RIXS SPECTRA OF T' CUPRATES

Figure 2(a) shows a representative Cu L_3 RIXS spectrum of AF-NCO measured with σ_{in} polarization, $\phi = 0^\circ$, and

$\mathbf{Q} = (0.34, 0, 1.27)$ reciprocal lattice units (r.l.u.). As has been experimentally observed [3–6,20,34], the low-energy RIXS spectrum of cuprates consists of elastic, magnon, and bimagnon (or multimagnon) peaks, respectively, which in AF-NCO are located at $\Delta E = 0, 0.27 \pm 0.02, 0.39 \pm 0.02$ eV (ΔE being the energy transfer: $E_{in} - E_{out}$). Note that the energy of the bimagnon peak observed here is consistent with a bimagnon energy of 0.38 and 0.43 eV measured by optical Raman scattering and Cu K edge RIXS in the closely related compound La₂CuO₄ [2,43]. As illustrated in Fig. 2(b), low-energy excitations in SC-NCO remain similarly well resolved despite the (para-)magnon and bimagnon peaks becoming broader due to a doping-induced breakdown of long-range magnetic order [3–6]. In Fig. 2(c), we also show the dd excitation peaks from AF-NCO, which exhibit orbital components that appear well separated compared to other cuprates [44]. Considering the local D_{4h} symmetry of the Cu²⁺ ion, we assign the peaks at $\Delta E = 1.42, 1.67, 2.40$ eV [DD1, DD2, and DD4 in Fig. 2(c)] to d_{xy} , $d_{xz/yz}$, and $d_{3z^2-r^2}$ orbital excitations, respectively. The additional small peak near 1.95 eV (DD3) has been observed in other T' cuprates, such as CaCuO₂ and Sr₂CuO₂Cl₂, but the origin of this additional excitation is still under debate [44].

Before discussing the detailed azimuthal dependence of RIXS spectra and the comparison between experimental data and theoretical calculations, we remark that the self-absorption of scattered photons has to be accounted within the quantitative analysis of the x-ray scattering intensities in different geometries [45]. In our case, the measured atomic form factor allows us to calculate the effect of self-absorption as a function of experimental geometry and energy transfer, as in Refs. [36,37]. In Appendix C, we present the detailed procedure for the self-absorption correction that was applied to our RIXS spectra. At the same time, we emphasize that the intensity variation in our experiment is clearly distinctive across different excitations and polarizations even before the self-absorption corrections (Appendix D). Thus, we can firmly rule out that self-absorption effects, which depend mainly on the experimental geometry, might hinder the reliability of our analysis [45]. All the data presented below are corrected for self-absorption accordingly.

IV. AZIMUTHAL DEPENDENCE OF THE LOW-ENERGY RIXS SPECTRA

The applicability of our approach is apparent from the pronounced azimuthal variation of the individual excitations in the RIXS spectra. This can be clearly appreciated from Figs. 3(a) and 3(b), which showcases the azimuthal dependence of the low-energy RIXS spectra of AF-NCO measured with σ_{in} and π_{in} polarized incoming light, respectively. Figures 3(c) and 3(d) displays a sample of individual spectra at four representative azimuthal angles $0^\circ, 90^\circ, 180^\circ$, and 270° . In the case of σ_{in} incoming polarization, it is clear from both the two-dimensional map, Figs. 3(a) and 3(b), and the peak decomposition of individual spectra, Figs. 3(c) and 3(d), that the cross section for elastic scattering is maximized at 0° and 180° and minimized near 90° and 270° . In stark contrast, the magnon intensity shows a maximum at 0° and a minimum at 180° with a doubled azimuthal periodicity compared to the

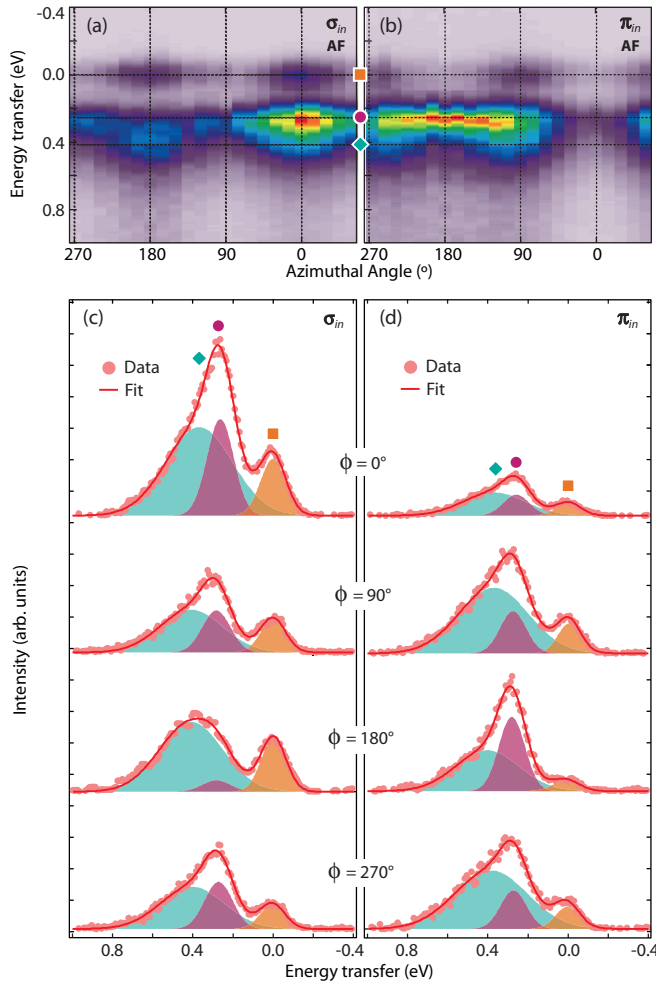


FIG. 3. (a) and (b) Azimuthal dependence of low-energy RIXS spectra of AF-NCO measured with σ and π incoming polarizations at $\mathbf{Q} = (0.34, 0, 1.27)$ r.l.u. Positions of elastic, magnon, and bimagnon peaks at $\phi = 0^\circ, 90^\circ, 180^\circ,$ and 270° are marked using orange, magenta, and green markers for guidance. (c) and (d) Fitting of RIXS spectra at four representative azimuthal angles: $\phi = 0^\circ, 90^\circ, 180^\circ,$ and 270° .

elastic signal. With π_{in} polarization, the positions of maxima and minima are reversed, whereas the periodicity for each excitation is preserved.

In Figs. 4(a)–4(c), we summarize the azimuthal dependence of low-energy excitations of AF-NCO. For comparison, in Figs. 4(g) and 4(h), we simulate the azimuthal dependence of elastic scattering and magnon excitations based on the scattering tensors obtained within the single-ion approximation (see the appendices for the details of the calculations). Overall, the distinctive azimuthal dependences observed for different excitations are well reproduced by the calculation for both polarizations.

The scattering tensors for elastic scattering (nonspin flip) and magnon excitations (single spin flip) have the following form in the cuprates:

$$F_{\text{elastic}} = \begin{pmatrix} 2 & 0 & 0 \\ 0 & 2 & 0 \\ 0 & 0 & 0 \end{pmatrix}, \quad F_{\text{magnon}} = \begin{pmatrix} 0 & i & 0 \\ -i & 0 & 0 \\ 0 & 0 & 0 \end{pmatrix}.$$

As expected, F_{elastic} is reduced to a diagonal tensor since there is no transfer of photon angular momentum to the sample for elastic scattering. In contrast, magnetic excitations require transfer of the photon angular momentum to the spin degree of freedom via core-hole spin-orbit coupling. Thus, F_{magnon} has nonzero off-diagonal components only [9]. We note that our form of F_{magnon} in the single-ion approximation agrees with the general spin excitation tensor in the cuprates [10].

An intuitive way to understand how different realizations of the scattering tensor are imprinted in the azimuthal dependence of the RIXS intensity is to consider the symmetries of the RIXS process. In the case of pure charge excitations, the intensity is dominated by polarization preserving ($\sigma \rightarrow \sigma'$ and $\pi \rightarrow \pi'$) channels. Thus, for most scattering events, the mirror symmetry on the scattering plane with respect to the scattering wave-vector \mathbf{Q} is preserved. The resulting symmetry between $I(\phi)$ and $I(180^\circ - \phi)$ forces the occurrence of two minima and two maxima over the full azimuthal range (0° – 360°). In contrast, for excitations with a single spin flip, the intensity is dominated by polarization flipping ($\sigma \rightarrow \pi'$ and $\pi \rightarrow \sigma'$) channels which break the mirror symmetry with respect to \mathbf{Q} . This gives rise to doubled periodicity of the intensity of (para)magnon excitations compared to purely elastic scattering (charge) as clearly observed in our experiment.

The azimuthal dependence of the bimagnon excitation is expected to exhibit a mixed chargelike and spinlike character. In fact, as shown in Fig. 4(c), the azimuthal dependence of the bimagnon intensity displays two minima and maxima but with a clear asymmetry between $\phi^\circ = 0$ and $\phi^\circ = 180$ for both polarizations. This behavior can be reproduced by a superposition of charge and spin scattering as depicted in Fig. 4(i). This fitting of the azimuthal dependence allows us to reliably estimate the relative contribution of charge and spin spectral weight to be 2.7 ± 0.2 . The dominance of chargelike ($\Delta S = 0$) processes in the bimagnon spectral weight naturally explains the resemblance of bimagnon spectra of La_2CuO_4 measured at the $\text{Cu } L_3$ and $\text{Cu } K$ edges where in the latter case only $\Delta S = 0$ bimagnon excitations are allowed [46].

In Fig. 5, we extended our analysis to the doped cuprates SC-NCO and YBCO. In the case of SC-NCO, the azimuthal dependence of elastic scattering, paramagnon excitation, and bimagnon excitation excellently agrees with the result from AF-NCO. Our results strongly support the hypothesis that the (para)magnon and bimagnon peaks in SC-NCO possess the same character as in the parent insulator. At the same time, fitting to azimuthal dependence of bimagnon excitation in SC-NCO reveals that the charge-to-spin ratio slightly increased with doping (from 2.7 ± 0.2 to 3.0 ± 0.2), indicating the additional contribution to the charge spectral weight from doped carriers (see also Sec. VI) [17–19].

In the case of YBCO, we used the experimental geometry that locks the in-plane momentum transfer (\mathbf{Q}_\parallel) at the charge order wave-vector $h \sim 0.33$ r.l.u. where the RIXS spectrum is characterized by a pronounced enhancement of the elastic line as illustrated in Fig. 5(d) [47]. The azimuthal dependence of the elastic scattering intensity of YBCO shows two minima/maxima as expected for charge scattering, although the intensity is partly suppressed near $\phi = 180^\circ$ due to a slight misalignment between in-plane momentum transfer and the

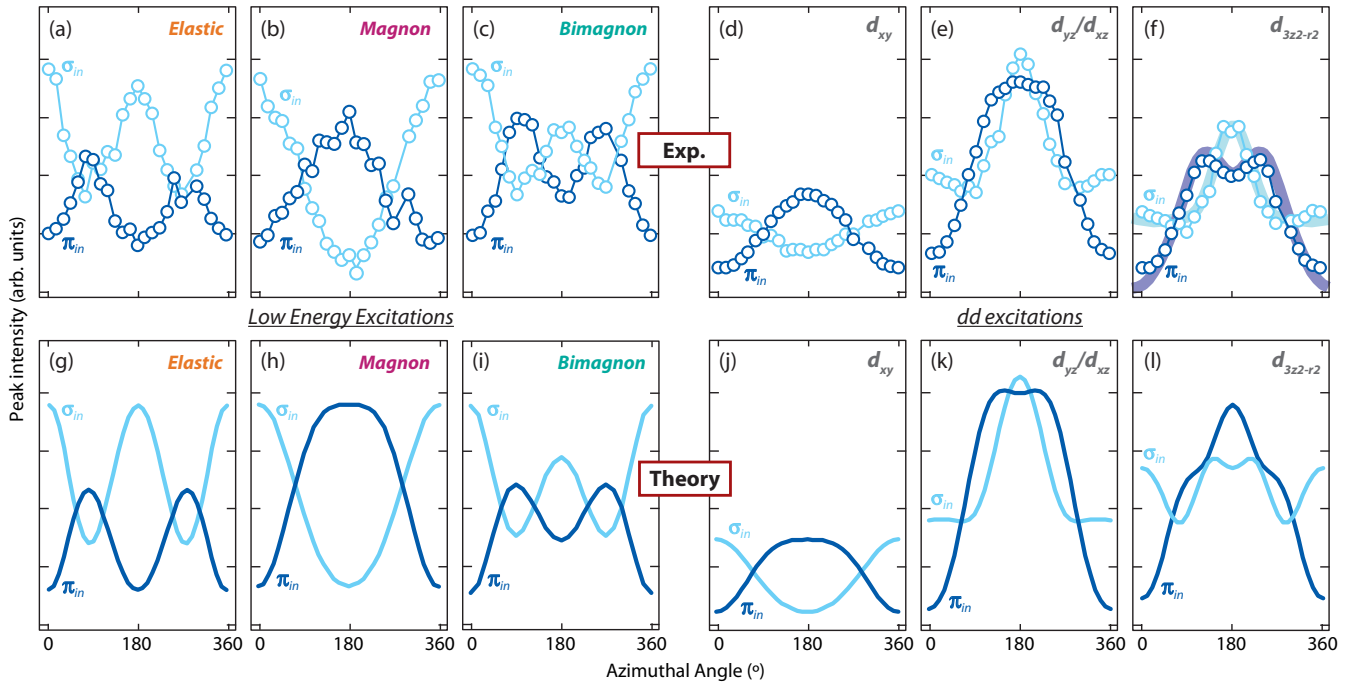


FIG. 4. (a)–(c), Azimuthal dependence of low-energy excitations of AF-NCO. Light blue (dark blue) open circles represent data measured with σ (π) polarizations. (d)–(f) Azimuthal dependence of dd excitations of AF-NCO. (g)–(l) Corresponding calculations of azimuthal angle-dependent RIXS intensity under the single-ion approximation. The thick lines in (f) show the calculation of azimuthal dependence of $d_{3z^2-r^2}$ excitation for the spin-flip channel only (see the text for details).

exact charge order wave vector [48]. On the other hand, the azimuthal dependence of the paramagnon intensity in YBCO quantitatively agrees with that of AF-NCO and SC-NCO. In conclusion, the characteristic azimuthal dependence of charge and spin excitations shows high consistency across all samples investigated, confirming the high reliability of our methods.

V. AZIMUTHAL DEPENDENCE OF THE ORBITAL EXCITATIONS

With the sensitivity to the detailed azimuthal dependence of low-energy excitations, our method can be further applied to resolve the excitations with a more complex scattering tensor. In cuprates, this is the case for the dd excitations at

higher energies where the scattering matrices are intrinsically asymmetric and contain a larger number of nonvanishing matrix elements: For example, the scattering matrix for non-spin-flip excitation from $d_{x^2-y^2}$ to d_{xz} is

$$F_{d_{x^2-y^2} \rightarrow d_{xz}} = \begin{pmatrix} \frac{1}{2} & \frac{i}{2} & 0 \\ -\frac{i}{2} & -\frac{1}{2} & 0 \\ \frac{1}{2} & -\frac{3i}{2} & 0 \end{pmatrix}.$$

The pronounced asymmetry is due to the different orbital quantum numbers between initial and final states, which forces the RIXS process to occur via transfer of photon angular momentum to orbital angular momentum. This results in the complex azimuthal dependence of RIXS intensity as

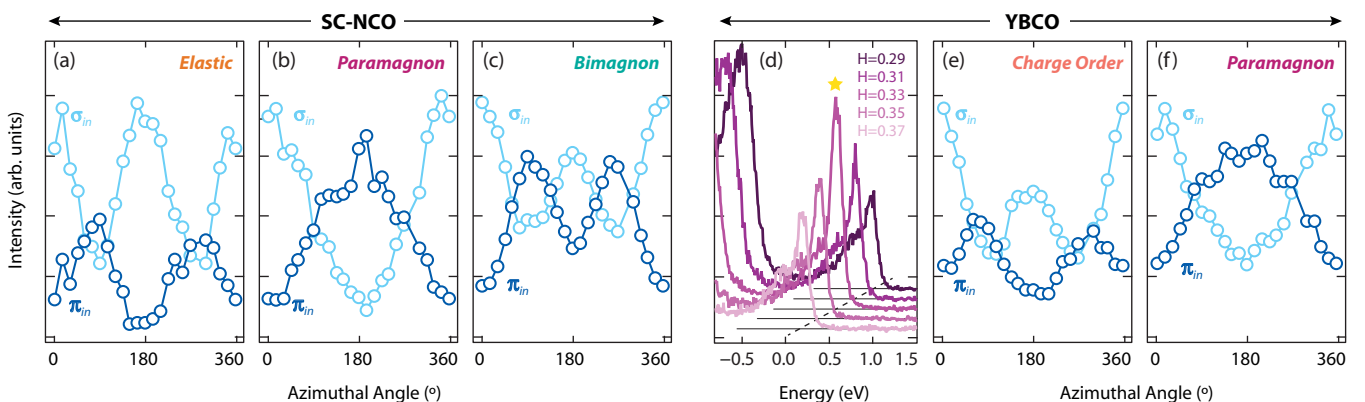


FIG. 5. (a)–(c) Azimuthal dependence of elastic scattering, paramagnon excitation, and bimagnon excitation in SC-NCO. (d) Low-energy excitations of YBCO around the charge order wave vector. (e) and (f) Azimuthal dependence of the charge order scattering and the paramagnon excitation in YBCO.

calculated in Figs. 4(j)–4(l). Through this analysis, we can assign the experimentally observed azimuthal dependence of d_{xy} and d_{yz}/d_{xz} excitations to corresponding calculations for different orbital excitations as displayed in Figs. 4(d) and 4(e). The excellent agreement demonstrates that our approach is not limited to the charge and spin excitations and is applicable in resolving the excitations involving complex and very general (or low-symmetric) form of the scattering tensor.

It is worth noting that the azimuthal dependence of the $d_{3z^2-r^2}$ excitation shows an ostensible discrepancy with the calculation. The deviation from the calculation is manifested differently for the σ_{in} and π_{in} polarization channels (for example, the experimental intensity at $\phi = 180^\circ$ appears to be higher than the calculation in the σ_{in} channel, whereas it is lower in the π_{in} channel), so we rule out any geometrical causes (for example, inaccuracies in the self-absorption correction). Rather, this unexpected azimuthal dependence might reflect an intrinsic property of the sample. Surprisingly, the experimental azimuthal dependence can be perfectly reproduced if we only account the $d_{3z^2-r^2}$ excitation with the spin flip, shown as a thick line in Fig. 4(f). This implies that the spin-conserving $d_{x^2-y^2} \rightarrow d_{3z^2-r^2}$ excitation is intrinsically suppressed on the CuO plane. The origin of this unexpected behavior of $d_{3z^2-r^2}$ orbital excitation in the T' cuprate might be beyond the single-ion approximation and will be the subject of future theoretical studies.

We also investigated the azimuthal dependence of the additional peak observed in the dd excitation region [DD3 in Fig. 2(c)] to shed new light on its origin. This additional peak has also been observed in other T' -structured cuprates, but its nature has remained unclear [44]. Previously, it has been suggested to originate from random oxygen vacancies that affect the local electronic structure of Cu^{2+} [44]. However, in our case, the peak appears in both as-grown AF-NCO and two-step oxygen-annealed SC-NCO with nearly equal intensity, suggesting that this excitation might not be related to random oxygen vacancies. Moreover, the peak has a systematic azimuthal dependence (Appendix E), implying that it arises from an excitation with a well-defined spin/orbital symmetry, rather than just random defects. Combined with the unexpected azimuthal dependence of $d_{3z^2-r^2}$ excitation, this shows that there might be rich but yet unexplored physics behind the dd excitation part of the RIXS spectrum of T' cuprates.

Altogether, the broad agreement between experiment and theory for charge, spin, and orbital excitations demonstrates that azimuthal angle-dependent RIXS can be used to unfold the contribution of multiple elements of the scattering matrix. The proposed approach can be used to identify the character of local and collective excitations in several materials with coupled spin/charge/orbital degrees of freedom, such as cobaltates, Fe-based superconductors, orbital-ordered manganites, and spin-orbit coupled $5d$ oxides [15,16,27,28,30–32].

VI. DISENTANGLING THE RIXS SPECTRA IN TERMS OF THE NATURE OF EXCITATIONS

In the last part of our analysis, we extend the machinery developed thus far to extract the chargelike ($\Delta S = 0$) and spinlike ($\Delta S = 1$) components of the RIXS spectrum.

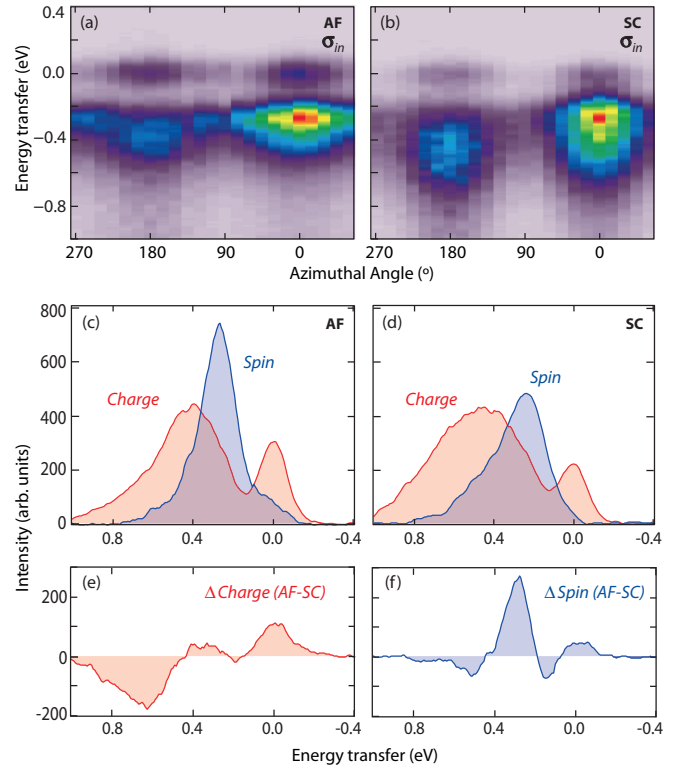


FIG. 6. (a) and (b) Azimuthal dependence of RIXS spectra of AF-NCO and SC-NCO measured with σ incoming polarization at $\mathbf{Q} = (0.34, 0, 1.27)$ r.l.u. (c) and (d) Disentangled intensity of chargelike and spinlike excitations in RIXS spectra of AF-NCO and SC-NCO. (e) and (f) Difference of the spin and charge spectral distribution of AF-NCO and SC-NCO.

Figures 6(a) and 6(b) report the azimuthal dependence of the RIXS spectra of AF-NCO and SC-NCO measured with incident σ polarized light. Using these (E, ϕ) RIXS maps, we can separate the charge and spin contributions from the RIXS azimuthal dependence (at every value of energy transfer) using the following equation:

$$I(E, \phi) = w_c(E)I_c(\phi) + w_s(E)I_s(\phi). \quad (1)$$

Here $I_{c(s)}(\phi)$ is the calculated azimuthal dependence of the charge (spin) excitation intensity [Figs. 4(g) and 4(h)], and $w_{c(s)}(E)$ is the fitting parameter representing the respective weight of charge (spin) at each energy transfer. Considering the similarity of $I_{c(s)}(\phi)$ with the $\cos 2\phi$ ($\cos \phi$) function, this procedure is similar to the Fourier transform in the ϕ domain where the $\pi(2\pi)$ periodic component represents the weight from the charge (spin) channel. As displayed in Figs. 6(c) and 6(d) the spin and charge components of the RIXS intensity can be effectively extracted using this method. The chargelike contribution dominates the intensity of the elastic scattering and bimagnon excitation, whereas spin excitations sharply peak at the single magnon/paramagnon energy. We note that the former and the latter show strong resemblances to the RIXS spectra of Ce-doped bulk NCO measured in $\sigma \rightarrow \sigma$ and $\sigma \rightarrow \pi$ polarization channels, respectively [49]. Additionally, our approach accurately captures subtle features, such as an asymmetry in the spin spectral distribution (SD)

near 400 meV due to spin contributions within the bimagnon excitations, and the broadening of magnetic excitations in SC-NCO due to the damping by the Stoner excitation [3–6]. This finding underscores the high sensitivity of azimuthal angle-dependent RIXS in resolving the character of electronic excitations even in the presence of substantial spectral overlap.

The present method enables to separately track down the evolution of the spectral distribution from chargelike and spinlike excitations as a function of doping. This information is pivotal to understand the role of low-energy excitations in the framework of high-temperature superconductivity. The mixed spin-charge character of the bimagnon peak also indicates that the spin and charge channels cannot be simply separated by isolating the magnon and bimagnon features but require a more detailed analysis of the kind discussed in this paper. In Figs. 6(e) and 6(f), we present the SD difference between AF-NCO and SC-NCO ($\Delta SD = SD_{AF} - SD_{SC}$) in the charge and spin channels. The main finding is that the spin and charge spectral distributions are unequally affected by doping: In the superconducting phase, the total spin spectral weight decreases by $\approx 10\%$, whereas the charge spectral weight increases by a similar amount. The difference of spectral distribution in the spin channel displays a positive peak at the single (para-)magnon energy and two-side minima, which likely arise from the broadening of both (para-)magnon and spinlike bimagnon excitations upon doping. Except for the slight broadening, the shape and weight of the spin SD of AF-NCO largely survives in SC-NCO, consistent with the persistence of spin fluctuations in the superconducting regime [3–6]. In contrast, we observe additional spectral weight in the charge channel of SC-NCO at high energies (from 0.5 to 1 eV), which cannot be attributed to the broadening of chargelike bimagnon excitations ($\Delta S = 0$). Instead, this spectral weight might originate from additional contributions due to particle-hole excitations in the doped compound as suggested in recent theoretical studies [18,19]. The energy scale of this particle-hole contribution is similar to that of the broad continuum in overdoped YBCO which exhibits fluorescence behavior [20].

VII. SUMMARY

To summarize, we have demonstrated a systematic method to resolve the charge, spin, and orbital character of the electronic excitations in RIXS spectra. In the study of prototypical cuprate compounds, we observed distinct azimuthal dependences of elastic scattering, (para-)magnon/bimagnon excitations, and dd excitations and find them in excellent agreement with theoretical calculations within the single-ion approximation. Ultimately, our method has been used to disentangle the spin and charge contributions to the low-energy RIXS spectra of cuprates. The ability to track down the evolution of the chargelike and spinlike characters of excitations from the antiferromagnetic to the superconducting regime reveals important information on the excitations that are more strongly coupled to the electronic states on the CuO planes. The method presented in this paper introduces a different way to use RIXS to resolve the character of electronic excitations

in a wide range of quantum materials with entangled charge, spin, and orbital degrees of freedom.

ACKNOWLEDGMENTS

We thank S. Todadri and K. Wohlfeld for insightful discussions. We acknowledge G. H. Zhang for supporting calculations. We thank L. Nue for help with manufacturing the wedged-sample holders. We acknowledge the Paul Scherrer Institut for the provision of synchrotron radiation beam time at the ADDRESS beamline of the Swiss Light Source. M.K. acknowledges a Samsung Scholarship from the Samsung Foundation of Culture. J.P. was financially supported by the Swiss National Science Foundation Early Postdoc, and Postdoc Mobility Fellowship Projects No. P2FRP2_171824 and No. P400P2_180744, E.P. was financially supported by the Swiss National Science Foundation (SNSF) through the Snergia Network Mott Physics Beyond the Heisenberg (MPBH) model, and D.E.M. was supported by the NCCR MARVEL of SNSF. This work was supported by the STC Center for Integrated Quantum Materials, NSF Grant No. DMR-1231319.

M.K. and J.P. contributed equally to this work.

APPENDIX A: SCATTERING MATRICES OF CHARGE/SPIN/ORBITAL EXCITATIONS IN RIXS

In RIXS, the intensity of the scattered electric field can be expressed as

$$I(\omega_k, \omega'_k, \mathbf{k}, \mathbf{k}', \epsilon, \epsilon') = \sum_f |F(\omega_k, \omega'_k, \mathbf{k}, \mathbf{k}', \epsilon, \epsilon')| \times \delta(E_f + \hbar\omega_k - E_g - \hbar\omega'_k), \quad (\text{A1})$$

where ω_k , \mathbf{k} , and $\epsilon(\omega_k, \mathbf{k}, \epsilon')$ represent the energy, the momentum, and the polarization of the incident (outgoing) light and F is the RIXS scattering amplitude [1]. The summation runs over all possible final-states f , and the δ function enforces the energy conservation explicitly.

In T' cuprates, the Cu^{2+} ion is surrounded by four oxygen ions and has D_{4h} point-group symmetry. Under the single-ion approximation and the dipole approximation, the RIXS intensity for each final state at the $\text{Cu } L_3$ edge is proportional to the following matrix elements which in the second-order perturbation expansion reads:

$$I_f^{\text{RIXS}}(\epsilon, \epsilon') \propto \left| \sum_i \langle f | D_{\epsilon'}^\dagger | i \rangle \langle i | D_\epsilon | g \rangle \right|^2 = \left| \sum_m \langle f | D_{\epsilon'}^\dagger | 2p_{3/2,m} \rangle \langle 2p_{3/2,m} | D_\epsilon | g \rangle \right|^2, \quad (\text{A2})$$

where $|g\rangle$, $|i\rangle$, and $|f\rangle$ represent the ground state, the intermediate state with a core hole, and the final state, respectively, and D_ϵ is a dipole operator. In cuprates, Cu spins are antiferromagnetically aligned along the Cu-O bond direction [50], therefore state $d_{x^2-y^2}^\uparrow$ can be rewritten as $(d_{x^2-y^2}^{\uparrow z} + d_{x^2-y^2}^{\downarrow z})/\sqrt{2}$. Depending on the final state, the above equation describes the elastic scattering for $|f\rangle = 3d_{x^2-y^2}^\uparrow$, the spin

excitations for $|f\rangle = 3d_{x^2-y^2}^\downarrow$, and the orbital + spin excitations for $|f\rangle = 3d_{xy}, 3d_{xz}, 3d_{yz}, 3d_{3z^2-r^2}$. In the calculation of the intensity of orbital excitations, we summed over all possible final spin states since the spin splitting for the dd excitation is not resolved in our experiment. Theoretically, this can be justified by the fact that the superexchange coupling J is orbital dependent and negligible except for the $d_{x^2-y^2}$ orbitals [44].

Based on the above equation, we can express the scattering matrices in the sample frame. For elastic scattering and magnon excitations, the orbital symmetry is preserved, and the resulting matrix (F_{elastic} and F_{magnon}) has a relatively simple form as described in Sec. IV. The scattering tensor for orbital excitations is more complex and asymmetric due to the change in orbital symmetry before and after the scattering event. For example, the $d_{3z^2-r^2}$ orbital excitation matrices for all possible spin channels are given as

$$F_{d_{x^2-y^2}^\uparrow \rightarrow d_{3z^2-r^2}^\uparrow} = \begin{pmatrix} 0 & -\frac{2i}{\sqrt{3}} & 0 \\ -\frac{2i}{\sqrt{3}} & 0 & 0 \\ 0 & \frac{2i}{\sqrt{3}} & 0 \end{pmatrix},$$

$$F_{d_{x^2-y^2}^\downarrow \rightarrow d_{3z^2-r^2}^\downarrow} = \begin{pmatrix} 0 & -\frac{2i}{\sqrt{3}} & 0 \\ -\frac{2i}{\sqrt{3}} & 0 & 0 \\ 0 & \frac{2i}{\sqrt{3}} & 0 \end{pmatrix},$$

$$F_{d_{x^2-y^2}^\uparrow \rightarrow d_{3z^2-r^2}^\downarrow} = \begin{pmatrix} -\frac{1}{\sqrt{3}} & 0 & 0 \\ 0 & \frac{1}{\sqrt{3}} & 0 \\ \frac{2}{\sqrt{3}} & 0 & 0 \end{pmatrix},$$

$$F_{d_{x^2-y^2}^\downarrow \rightarrow d_{3z^2-r^2}^\uparrow} = \begin{pmatrix} -\frac{1}{\sqrt{3}} & 0 & 0 \\ 0 & \frac{1}{\sqrt{3}} & 0 \\ -\frac{2}{\sqrt{3}} & 0 & 0 \end{pmatrix}.$$

As expected, the matrix elements representing a positive transfer of angular momentum from the sample to the photon (below diagonal) are nonzero, whereas those representing a negative transfer (above diagonal) become vanishing. This complexity of the orbital excitation tensor leads to a nontrivial azimuthal dependence of the RIXS intensity as discussed in Sec. V.

APPENDIX B: CALCULATION OF THE AZIMUTHAL DEPENDENCE OF RIXS INTENSITY

The above scattering matrices are defined in the sample frame, whereas the polarization vectors of incoming and outgoing photons are defined in the laboratory frame. Thus, we need an appropriate rotation matrix $R_{\text{tot}}(\theta_w, \phi, \theta)$ before projecting the scattering matrix onto the polarization vectors.

The total rotation matrix $R_{\text{tot}}(\theta_w, \phi, \theta)$ can be constructed from the four sequential rotation operations: R_o rotates the sample frame to the $\theta_w = \phi = \theta = 0$ position in the laboratory frame; R_w implements the transformation to the wedge-sample holder configuration; R_ϕ is responsible for the azimuthal rotation; and R_θ aligns the axis of the azimuthal rotation with the scattering wave vector $\mathbf{Q} = \mathbf{k}' - \mathbf{k}$. Therefore, we have $R_{\text{tot}}(\theta_w, \phi, \theta) = R_o R_w R_\phi R_\theta$. The angles θ_w , ϕ , and θ are defined in Fig. 7(a), and the schematics for each rotation

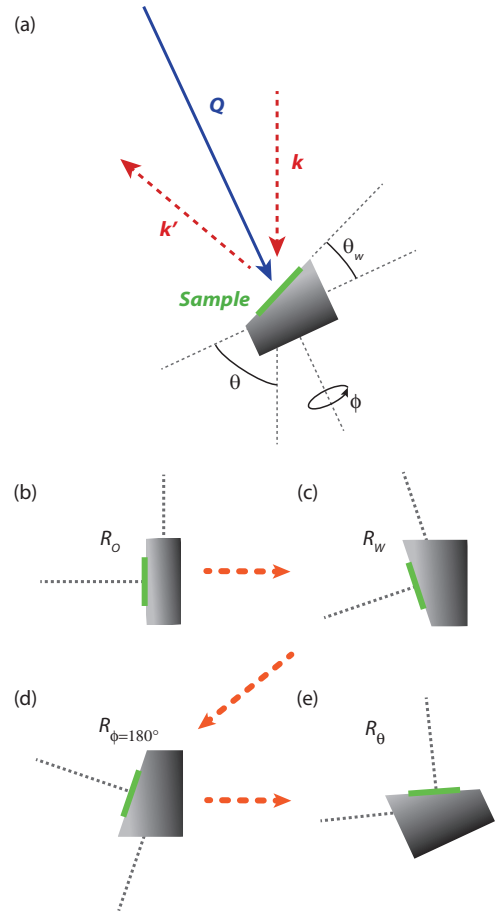


FIG. 7. (a) Scattering geometry of our experiment and definition of the rotation angles. (b)–(e) Schematics for the sequential operations of R_o , R_w , R_ϕ , and R_θ .

are shown in Figs. 7(b)–7(e). In our experiment, θ_w and θ are fixed at 40° and 65° , respectively, leaving ϕ as the only variable of R_{tot} . After applying the full rotation operation to the scattering tensor corresponding to each type of excitation, we can directly calculate the azimuthal dependence of the RIXS intensity as

$$I_f^{\text{RIXS}}(\epsilon, \phi) = \sum_{\epsilon'} |\epsilon' R_{\text{tot}}^T(\phi) F_f R_{\text{tot}}(\phi) \epsilon|^2. \quad (\text{B1})$$

Here, we sum the intensity over the polarization of the outgoing photons since the latter is not experimentally determined in the present experiment. The essence of azimuthal dependence analysis is that, via the action of the azimuthal angle-dependent unitary matrix $R_{\text{tot}}(\phi)$, the individual elements of the scattering tensor can be disentangled once projected to fixed polarization vectors. In other words, the form of the scattering tensor and thus the nature of the corresponding excitation are imprinted onto the dependence of $I_f^{\text{RIXS}}(\epsilon, \phi)$.

APPENDIX C: SELF-ABSORPTION CORRECTION IN RIXS

Self-absorption is an unavoidable contribution to the measured intensity of scattered x rays and depends on the experimental geometry and energy loss of the photons at a given incident photon energy. Generally, the removal of

self-absorption effects in the raw data is precluded in the absence of outgoing-polarization-resolved data. However, in our case, the effect of self-absorption can be exactly calculated in the model, given a specific form of the scattering tensor [36,37]. Specifically, the following formula is used to correct for self-absorption effects [45]:

$$I_{\text{corr}} = I_{\text{theory}} \left[\mu_{\text{in}}(E_{\text{in}}, \epsilon_{\text{in}}, \phi) + \mu_{\text{out}}(E_{\text{in}}, \epsilon_{\text{in}}, \phi) \frac{-\hat{k}_{\text{in}} \cdot \hat{n}(\phi)}{\hat{k}_{\text{out}} \cdot \hat{n}(\phi)} \right]^{-1} = I_{\text{theory}} C(E_{\text{in}}, \epsilon_{\text{in}}, E_{\text{out}}, \epsilon_{\text{out}}, \phi). \quad (\text{C1})$$

Here, μ_{in} and μ_{out} are the absorption coefficients for the incoming and outgoing light, respectively, and \hat{n} is the vector normal to the sample surface. The dot products of \hat{n} and \hat{k}_{in} or \hat{k}_{out} define the geometrical factor for the self-absorption correction. The ϕ dependence of the correction function C originates from the absorption coefficient as well as the geometrical factor.

The explicit dependence of the absorption coefficient on the experimental parameters can be written as

$$\mu_{\text{in(out)}} = \epsilon_{\text{in(out)}} \left[R^T(\phi) \begin{pmatrix} f_{aa}(E) & 0 & 0 \\ 0 & f_{aa}(E) & 0 \\ 0 & 0 & f_{cc}(E) \end{pmatrix} R(\phi) \right] \times \epsilon_{\text{in(out)}}. \quad (\text{C2})$$

In our experiment E_{in} is fixed to the energy of the Cu L_3 edge (in our case, 929.7 eV), but the emission energy of the photons E_{out} and, thus, $f_{aa}(E_{\text{out}})$ and $f_{cc}(E_{\text{out}})$ vary for different excitations. The energy-dependent values of f_{aa} and f_{cc} can be obtained from x-ray absorption spectra (total electron yield) collected at different polarizations. In Fig. 8(a), we show the absorption spectra of the parent Nd_2CuO_4 (AF-NCO) overlapped with the excitation spectrum from RIXS. The f_{cc}/f_{aa} ratio is minimum at the peak of the absorption spectrum and approaches unity for higher-energy transfers. For example, $f_{cc}/f_{aa} = 0.36$ for elastic scattering, and $f_{cc}/f_{aa} = 0.63$ for the d_{xy} excitation.

Figures 8(b) and 8(c) show the dependence of the absorption coefficient on the polarization and azimuthal angle for different values of f_{cc}/f_{aa} [corresponding to different excitations in the RIXS spectrum of Fig. 8(a)]. The variation with azimuthal angle is maximized for small f_{cc}/f_{aa} and is suppressed as f_{cc}/f_{aa} approaches unity for high-energy excitations. The azimuthal dependence of μ possesses mirror symmetry with respect to $\phi = 180^\circ$ due to the mirror symmetry relative to the scattering plane. Additionally, the profiles of $\mu_{\pi\text{in}}$ and $\mu_{\pi\text{out}}$ are shifted by 180° due to mirror symmetry with respect to scattering wave-vector \mathbf{Q} .

Figures 8(d) and 8(e) display the calculated correction factor C for elastic scattering and for d_{xy} excitations. Overall, the effect of self-absorption correction is maximized for a grazing emission geometry ($\phi = 180^\circ$) and minimized for a grazing incidence geometry ($\phi = 0^\circ$) as expected. The outgoing polarization dependence of C is suppressed at high f_{cc}/f_{aa} , curves with different outgoing polarizations, and eventually collapses onto a single curve when $f_{cc}/f_{aa} = 1$.

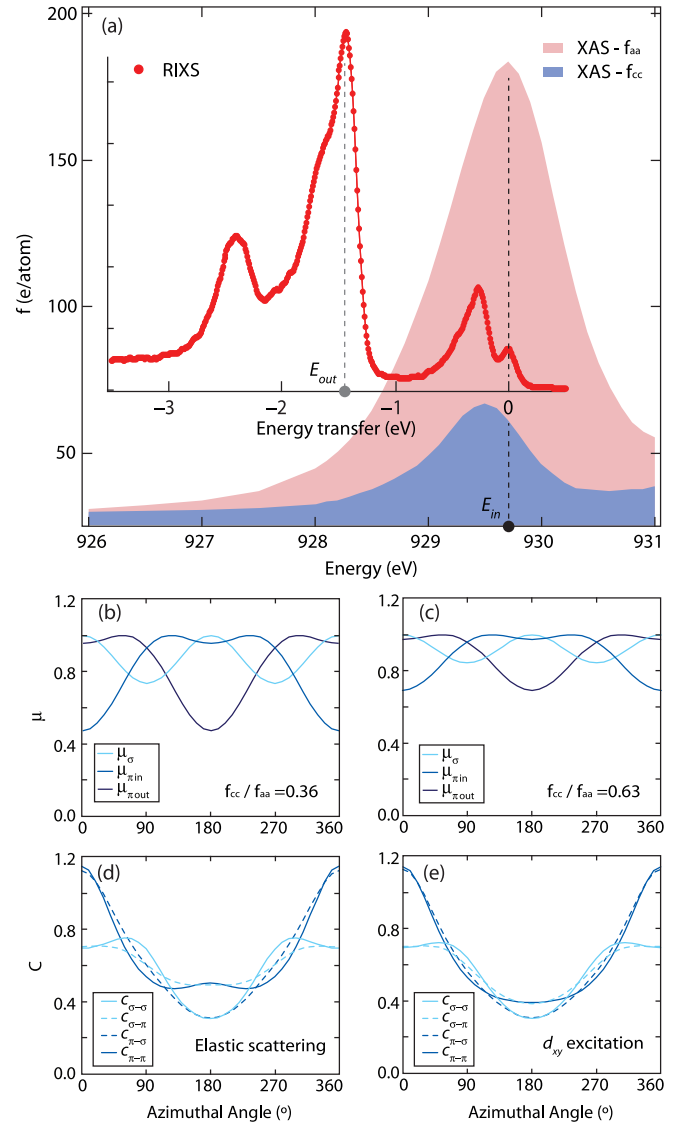


FIG. 8. (a) XAS and RIXS spectra of AF-NCO. (b) and (c) Azimuthal dependence of the absorption coefficients for $f_{cc}/f_{aa} = 0.36$ and $f_{cc}/f_{aa} = 0.63$. (d) and (e) Azimuthal dependence of the self-absorption correction factors for elastic scattering and d_{xy} orbital excitation.

To calculate the RIXS intensities for σ and π incoming polarizations, the self-absorption correction should be applied separately to each polarization channel as follows:

$$I_{\sigma}^{\text{corr}}(\phi) = I_{\sigma \rightarrow \sigma} C_{\sigma \rightarrow \sigma} + I_{\sigma \rightarrow \pi} C_{\sigma \rightarrow \pi}, \quad (\text{C3})$$

$$I_{\pi}^{\text{corr}}(\phi) = I_{\pi \rightarrow \sigma} C_{\pi \rightarrow \sigma} + I_{\pi \rightarrow \pi} C_{\pi \rightarrow \pi}. \quad (\text{C4})$$

With the exact knowledge of $I_{\sigma(\pi) \rightarrow \sigma}$ and $I_{\sigma(\pi) \rightarrow \pi}$ from the calculation (see Appendices A and B), we can combine $C_{\sigma(\pi) \rightarrow \sigma}$ and $C_{\sigma(\pi) \rightarrow \pi}$ to the single factor $C_{\sigma(\pi)}$, which depends only on the incoming polarization,

$$I_{\sigma(\pi)}^{\text{corr}} = [I_{\sigma(\pi) \rightarrow \sigma} + I_{\sigma(\pi) \rightarrow \pi}] \times \frac{I_{\sigma(\pi) \rightarrow \sigma} C_{\sigma(\pi) \rightarrow \sigma} + I_{\sigma(\pi) \rightarrow \pi} C_{\sigma(\pi) \rightarrow \pi}}{[I_{\sigma(\pi) \rightarrow \sigma} + I_{\sigma(\pi) \rightarrow \pi}]} = I_{\sigma(\pi)}(\phi) C_{\sigma(\pi)}(\phi). \quad (\text{C5})$$

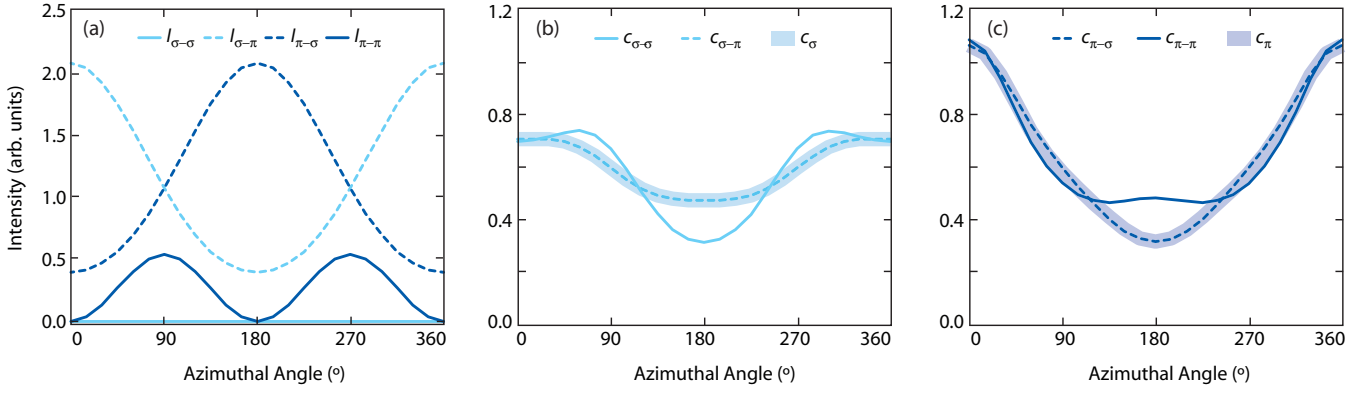


FIG. 9. (a) Calculated (para-)magnon intensities for different polarization channels. (b) and (c) Outgoing-polarization-resolved and total self-absorption correction factors for σ and π incoming polarizations.

In Fig. 9, we report an example of the procedure outlined above. Figure 9(a) shows the calculated (para-)magnon intensity for each incoming and outgoing polarization. The RIXS intensity of (para-)magnon excitations is dominated by cross-polarization channels as expected. The intensity of $\sigma \rightarrow \sigma$ scattering vanishes for all azimuthal angles as the scattering processes in this channel do not transfer photon angular momentum to the sample. In contrast, the $\pi \rightarrow \pi$ scattering channel is active since π_{in} and π_{out} are not parallel to each other. In Figs. 9(b) and 9(c), we plot the outgoing-polarization-resolved correction factors $C_{\sigma(\pi) \rightarrow \sigma}(\phi)$ and $C_{\sigma(\pi) \rightarrow \pi}(\phi)$ as well as the total self-absorption correction factors $C_{\sigma(\pi)}(\phi)$ calculated from the above equation.

In the main text, we divided the experimental data by $C_{\sigma(\pi)}(\phi)$ instead of imposing its effect on theory. By this, we remove the effect of self-absorption and present the azimuthal dependence arising purely from charge/spin/orbital excitations.

APPENDIX D: RAW RIXS SPECTRA OF AF-NCO AND THE FITTING PROCEDURE

Figure 10 includes the complete azimuthal series of low-energy RIXS spectra of AF-NCO before the self-absorption correction. We note that the total acquisition time for a full azimuthal series is comparable to that of outgoing-polarization-resolved RIXS experiments considering the current efficiency of the outgoing-polarization filter [51]. The spectra were measured with σ incoming polarization. Overall, the intensity is enhanced near $\phi = 0^\circ$ and suppressed near $\phi = 180^\circ$, which is the expected behavior in the presence of the self-absorption effects (see Fig. 8).

We fit the spectrum with a linear background and three Gaussian peaks. During the fitting process, we restrict the width of each peak to be constant across all the spectra for different ϕ 's. Spectra at all different azimuthal angles can be well fit with $\Delta E = 0, 0.27 \pm 0.02, 0.39 \pm 0.02$ eV, corresponding to elastic scattering, magnon excitations, and bimagnon excitations, respectively.

Even without self-absorption correction, we can capture the difference in the azimuthal dependence of each peak. For example, the magnon excitation intensity is almost completely suppressed near $\phi = 180^\circ$, whereas a substantial portion of

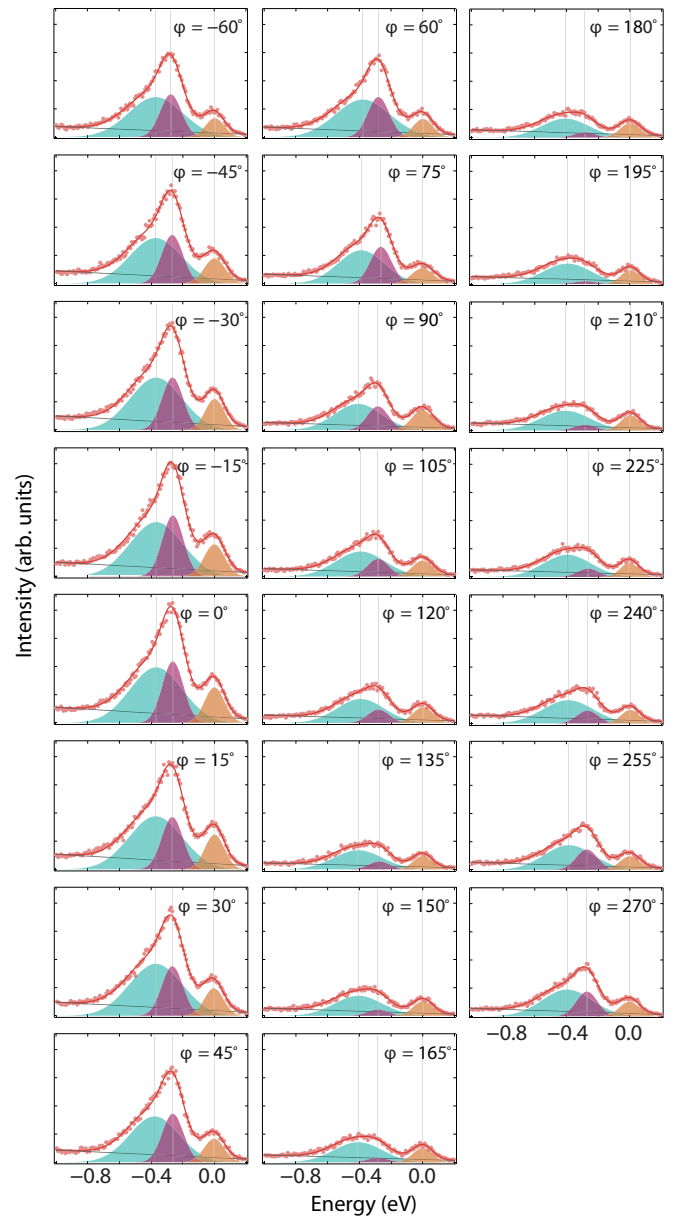


FIG. 10. Low-energy RIXS spectra of AF-NCO measured with σ incoming polarization under azimuthal rotation.

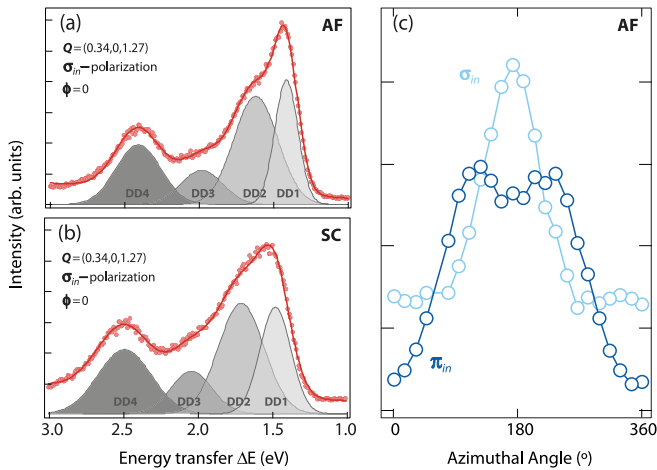


FIG. 11. (a) and (b) dd -excitation region of AF-NCO and SC-NCO. Data are measured at $\phi = 0^\circ$ with incoming σ polarization. (c) Azimuthal dependence analysis of the 1.95-eV peak in AF-NCO.

intensity remains in the cases of elastic scattering and bi-magnon scattering. In contrast to the rapid and monotonic

suppression of the magnon excitation intensity from $\phi = 0^\circ$ to $\phi = 180^\circ$, the intensity of elastic scattering in the raw data is almost constant from $\phi = 90^\circ$ to $\phi = 270^\circ$, which can be interpreted as a result of the interplay between the self-absorption correction factor (Fig. 8) and the intrinsic modulation of the cross section (Fig. 4).

APPENDIX E: DOPING AND AZIMUTHAL DEPENDENCE OF THE ADDITIONAL PEAK

In Fig. 11, we display the RIXS spectra of high-energy dd excitation in AF-NCO and SC-NCO. The additional peak (marked as DD3) near the energy transfer ~ 2 eV equally appears in both samples with similar intensities. This indicates that an oxygen annealing process marginally affects the peak except for the slight broadening observed in all dd -excitation peaks. Figure 11(c) shows the azimuthal dependence of these peaks in AF-NCO. The systematic and nontrivial azimuthal dependence indicates that the peaks emerge from a well-defined (yet unknown) excitation rather than the random defects as previously suggested [44].

- [1] L. J. P. Ament, M. Van Veenendaal, T. P. Devereaux, J. P. Hill, and J. Van Den Brink, *Rev. Mod. Phys.* **83**, 705 (2011).
- [2] J. P. Hill, G. Blumberg, Y. J. Kim, D. S. Ellis, S. Wakimoto, R. J. Birgeneau, S. Komiyama, Y. Ando, B. Liang, R. L. Greene, D. Casa, and T. Gog, *Phys. Rev. Lett.* **100**, 097001 (2008).
- [3] M. L. Tacon, G. Ghiringhelli, J. Chaloupka, M. M. Sala, V. Hinkov, M. W. Haverkort, M. Minola, M. Bakr, K. J. Zhou, S. Blanco-Canosa, C. Monney, Y. T. Song, G. L. Sun, C. T. Lin, G. M. De Luca, M. Salluzzo, G. Khaliullin, T. Schmitt, L. Braicovich, and B. Keimer, *Nat. Phys.* **7**, 725 (2011).
- [4] M. P. M. Dean, G. Dellea, R. S. Springell, F. Yakhov-Harris, K. Kummer, N. B. Brookes, X. Liu, Y.-J. Sun, J. Strle, T. Schmitt, L. Braicovich, G. Ghiringhelli, I. Božović, and J. P. Hill, *Nature Mater.* **12**, 1019 (2013).
- [5] W. S. Lee, J. J. Lee, E. A. Nowadnick, S. Gerber, W. Tabis, S. W. Huang, V. N. Strocov, E. M. Motoyama, G. Yu, B. Moritz, H. Y. Huang, R. P. Wang, Y. B. Huang, W. B. Wu, C. T. Chen, D. J. Huang, M. Greven, T. Schmitt, Z. X. Shen, and T. P. Devereaux, *Nat. Phys.* **10**, 883 (2014).
- [6] K. Ishii, M. Fujita, T. Sasaki, M. Minola, G. Dellea, C. Mazzoli, K. Kummer, G. Ghiringhelli, L. Braicovich, T. Tohyama, K. Tsutsumi, K. Sato, R. Kajimoto, K. Ikeuchi, K. Yamada, M. Yoshida, M. Kurooka, and J. Mizuki, *Nat. Commun.* **5**, 3714 (2014).
- [7] M. P. M. Dean, R. S. Springell, C. Monney, K. J. Zhou, J. Pereira, I. Božović, B. Dalla Piazza, H. M. Rønnow, E. Morenzoni, J. van den Brink, T. Schmitt, and J. P. Hill, *Nature Mater.* **11**, 850 (2012).
- [8] J. Schlappa, K. Wohlfeld, K. J. Zhou, M. Mourigal, M. W. Haverkort, V. N. Strocov, L. Hozoi, C. Monney, S. Nishimoto, S. Singh, A. Revcolevschi, J.-S. Caux, L. Patthey, H. M. Rønnow, J. van den Brink, and T. Schmitt, *Nature (London)* **485**, 82 (2012).
- [9] L. J. P. Ament, G. Ghiringhelli, M. M. Sala, L. Braicovich, and J. van den Brink, *Phys. Rev. Lett.* **103**, 117003 (2009).
- [10] M. W. Haverkort, *Phys. Rev. Lett.* **105**, 167404 (2010).
- [11] G. Ghiringhelli, A. Piazzalunga, C. Dallera, T. Schmitt, V. N. Strocov, J. Schlappa, L. Patthey, X. Wang, H. Berger, and M. Grioni, *Phys. Rev. Lett.* **102**, 027401 (2009).
- [12] L. J. P. Ament, G. Khaliullin, and J. van den Brink, *Phys. Rev. B* **84**, 020403 (2011).
- [13] J. Schlappa, T. Schmitt, F. Vernay, V. N. Strocov, V. Ilakovac, B. Thielemann, H. M. Rønnow, S. Vanishri, A. Piazzalunga, X. Wang, L. Braicovich, G. Ghiringhelli, C. Marin, J. Mesot, B. Delley, and L. Patthey, *Phys. Rev. Lett.* **103**, 047401 (2009).
- [14] C. J. Jia, E. A. Nowadnick, K. Wohlfeld, Y. F. Kung, C.-C. Chen, S. Johnston, T. Tohyama, B. Moritz, and T. P. Devereaux, *Nat. Commun.* **5**, 3314 (2014).
- [15] K.-J. Zhou, Y.-B. Huang, C. Monney, X. Dai, V. N. Strocov, N.-L. Wang, Z.-G. Chen, C. Zhang, P. Dai, L. Patthey, J. van den Brink, H. Ding, and T. Schmitt, *Nat. Commun.* **4**, 1470 (2013).
- [16] J. Pellicciari, Y. Huang, T. Das, M. Dantz, V. Bisogni, P. O. Velasco, V. N. Strocov, L. Xing, X. Wang, C. Jin, and T. Schmitt, *Phys. Rev. B* **93**, 134515 (2016).
- [17] M. Guarise, B. D. Piazza, H. Berger, E. Giannini, T. Schmitt, H. M. Rønnow, G. A. Sawatzky, J. van den Brink, D. Altenfeld, I. Eremin, and M. Grioni, *Nat. Commun.* **5**, 5760 (2014).
- [18] D. Benjamin, I. Klich, and E. Demler, *Phys. Rev. Lett.* **112**, 247002 (2014).
- [19] M. Kanász-Nagy, Y. Shi, I. Klich, and E. A. Demler, *Phys. Rev. B* **94**, 165127 (2016).
- [20] M. Minola, G. Dellea, H. Gretarsson, Y. Y. Peng, Y. Lu, J. Porras, T. Loew, F. Yakhov, N. B. Brookes, Y. B. Huang, J. Pellicciari, T. Schmitt, G. Ghiringhelli, B. Keimer, L. Braicovich, and M. Le Tacon, *Phys. Rev. Lett.* **114**, 217003 (2015).

- [21] Y. F. Kung, E. A. Nowadnick, C. J. Jia, S. Johnston, B. Moritz, R. T. Scalettar, and T. P. Devereaux, *Phys. Rev. B* **92**, 195108 (2015).
- [22] C. Jia, K. Wohlfeld, Y. Wang, B. Moritz, and T. P. Devereaux, *Phys. Rev. X* **6**, 021020 (2016).
- [23] H. Y. Huang, C. J. Jia, Z. Y. Chen, K. Wohlfeld, B. Moritz, T. P. Devereaux, W. B. Wu, J. Okamoto, W. S. Lee, M. Hashimoto, Y. He, Z. X. Shen, Y. Yoshida, H. Eisaki, C. Y. Mou, C. T. Chen, and D. J. Huang, *Sci. Rep.* **6**, 19657 (2016).
- [24] M. P. M. Dean, *J. Magn. Magn. Mater.* **376**, 3 (2015).
- [25] H. Chen, D. P. Kumah, A. S. Disa, F. J. Walker, C. H. Ahn, and S. Ismail-Beigi, *Phys. Rev. Lett.* **110**, 186402 (2013).
- [26] V. Bisogni, S. Catalano, R. J. Green, M. Gibert, R. Scherwitzl, Y. Huang, V. N. Strocov, P. Zubko, S. Balandeh, J.-M. Triscone, G. Sawatzky, and T. Schmitt, *Nat. Commun.* **7**, 13017 (2016).
- [27] S. B. Wilkins, P. D. Spencer, P. D. Hatton, S. P. Collins, M. D. Roper, D. Prabhakaran, and A. T. Boothroyd, *Phys. Rev. Lett.* **91**, 167205 (2003).
- [28] J. Pellicciari, K. Ishii, M. Dantz, X. Lu, D. E. McNally, V. N. Strocov, L. Xing, X. Wang, C. Jin, H. S. Jeevan, P. Gegenwart, and T. Schmitt, *Phys. Rev. B* **95**, 115152 (2017).
- [29] J. Pellicciari, M. Dantz, Y. Huang, V. N. Strocov, L. Xing, X. Wang, C. Jin, and T. Schmitt, *Appl. Phys. Lett.* **109**, 122601 (2016).
- [30] T. Satoh, R. Iida, T. Higuchi, Y. Fujii, A. Koreeda, H. Ueda, T. Shimura, K. Kuroda, V. I. Butrim, and B. A. Ivanov, *Nat. Commun.* **8**, 638 (2017).
- [31] J. Kim, D. Casa, M. H. Upton, T. Gog, Y.-J. Kim, J. F. Mitchell, M. van Veenendaal, M. Daghofer, J. van den Brink, G. Khalullin, and B. J. Kim, *Phys. Rev. Lett.* **108**, 177003 (2012).
- [32] S. Calder, J. G. Vale, N. A. Bogdanov, X. Liu, C. Donnerer, M. H. Upton, D. Casa, A. H. Said, M. D. Lumsden, Z. Zhao, J. Q. Yan, D. Mandrus, S. Nishimoto, J. van den Brink, J. P. Hill, D. F. McMorrow, and A. D. Christianson, *Nat. Commun.* **7**, 11651 (2016).
- [33] X. Lu, D. E. McNally, M. Moretti Sala, J. Terzic, M. H. Upton, D. Casa, G. Ingold, G. Cao, and T. Schmitt, *Phys. Rev. Lett.* **118**, 027202 (2017).
- [34] L. Braicovich, M. Moretti Sala, L. J. P. Ament, V. Bisogni, M. Minola, G. Balestrino, D. Di Castro, G. M. De Luca, M. Salluzzo, G. Ghiringhelli, and J. van den Brink, *Phys. Rev. B* **81**, 174533 (2010).
- [35] K. Ishii, S. Ishihara, Y. Murakami, K. Ikeuchi, K. Kuzushita, T. Inami, K. Ohwada, M. Yoshida, I. Jarrige, N. Tatami, S. Niioka, D. Bizen, Y. Ando, J. Mizuki, S. Maekawa, and Y. Endoh, *Phys. Rev. B* **83**, 241101 (2011).
- [36] R. Comin, R. Sutarto, F. He, E. H. da Silva Neto, L. Chauviere, A. Frao, R. Liang, W. N. Hardy, D. A. Bonn, Y. Yoshida, H. Eisaki, A. J. Achkar, D. G. Hawthorn, B. Keimer, G. A. Sawatzky, and A. Damascelli, *Nature Mater.* **14**, 796 (2015).
- [37] A. J. Achkar, F. He, R. Sutarto, C. McMahan, M. Zwiebler, M. Hucker, G. D. Gu, R. Liang, D. A. Bonn, W. N. Hardy, J. Geck, and D. G. Hawthorn, *Nature Mater.* **15**, 616 (2014).
- [38] Y. Krockenberger, H. Irie, O. Matsumoto, K. Yamagami, M. Mitsuhashi, A. Tsukada, M. Naito, and H. Yamamoto, *Sci. Rep.* **3**, 2235 (2013).
- [39] Y. Krockenberger, H. Yamamoto, A. Tsukada, M. Mitsuhashi, and M. Naito, *Phys. Rev. B* **85**, 184502 (2012).
- [40] R. Liang, D. A. Bonn, and W. N. Hardy, *Phys. Rev. B* **73**, 180505 (2006).
- [41] V. N. Strocov, T. Schmitt, U. Flechsig, T. Schmidt, A. Imhof, Q. Chen, J. Raabe, R. Betemps, D. Zimoch, J. Krempasky, X. Wang, M. Grioni, A. Piazzalunga, and L. Patthey, *J. Synchrotron Radiat.* **17**, 631 (2010).
- [42] G. Ghiringhelli, A. Piazzalunga, C. Dallera, G. Trezzi, L. Braicovich, T. Schmitt, V. N. Strocov, R. Betemps, L. Patthey, X. Wang, and M. Grioni, *Rev. Sci. Instrum.* **77**, 113108 (2006).
- [43] K. B. Lyons, P. A. Fleury, J. P. Remeika, A. S. Cooper, and T. J. Negran, *Phys. Rev. B* **37**, 2353 (1988).
- [44] M. Moretti Sala, V. Bisogni, C. Aruta, G. Balestrino, H. Berger, N. B. Brookes, G. M. De Luca, D. Di Castro, M. Grioni, M. Guarise, P. G. Medaglia, F. Miletto Granozio, M. Minola, P. Perna, M. Radovic, M. Salluzzo, T. Schmitt, K. J. Zhou, L. Braicovich, and G. Ghiringhelli, *New J. Phys.* **13**, 043026 (2011).
- [45] A. J. Achkar, T. Z. Regier, H. Wadati, Y. J. Kim, H. Zhang, and D. G. Hawthorn, *Phys. Rev. B* **83**, 081106 (2011).
- [46] V. Bisogni, L. Simonelli, L. J. P. Ament, F. Forte, M. Moretti Sala, M. Minola, S. Huotari, J. van den Brink, G. Ghiringhelli, N. B. Brookes, and L. Braicovich, *Phys. Rev. B* **85**, 214527 (2012).
- [47] G. Ghiringhelli, M. L. Tacon, M. Minola, C. Mazzoli, N. B. Brookes, G. M. D. Luca, A. Frano, D. G. Hawthorn, F. He, T. Loew, M. M. Sala, D. C. Peets, M. Salluzzo, E. Schierle, R. Sutarto, G. A. Sawatzky, E. Weschke, B. Keimer, and L. Braicovich, *Science* **337**, 821 (2012).
- [48] Since we detect the suppression of the intensity at $\phi = 180^\circ$ for both σ and π incoming polarizations, we conclude that the in-plane momentum transfer is slightly off from the exact charge order wave vector (presumably due to a small offset in the tilt angle), a misalignment which leaves a mark particularly near $\phi = 180^\circ$. Note that the charge order peak is relatively sharp in YBCO (FWHM 0.03 r.l.u.), and thus the small offset in angle (1° , 0.02 r.l.u.) can substantially suppress the intensity of the charge order scattering (up to a factor of 2) as evident from Fig. 5(d).
- [49] E. H. da Silva Neto, M. Minola, B. Yu, W. Tabis, M. Bluschke, D. Unruh, H. Suzuki, Y. Li, G. Yu, D. Betto, K. Kummer, F. Yakhov, N. B. Brookes, M. Le Tacon, M. Greven, B. Keimer, and A. Damascelli, *Phys. Rev. B* **98**, 161114(R) (2018).
- [50] N. P. Armitage, P. Fournier, and R. L. Greene, *Rev. Mod. Phys.* **82**, 2421 (2010).
- [51] L. Braicovich, M. Minola, G. Dellea, M. Le Tacon, M. Moretti Sala, C. Morawe, J.-C. H. Peffen, R. Supruangnet, F. Yakhov, G. Ghiringhelli, and N. B. Brookes, *Rev. Sci. Instruments* **85**, 115104 (2014).